Advances in Geo-Energy Research

Vol. 20, No. 1, p. 16-26, 2026

Original article

Direct link between wettability and acoustic signature in granular porous media

Yangpu Chen[1,2], Li-Yun Fu[1,3]*, Tobias M. Müller[1,4]

[1]*State Key Laboratory of Deep Oil and Gas, China University of Petroleum (East China), Qingdao 266580, P. R. China*

[2]*School of Geosciences, China University of Petroleum (East China), Qingdao 266580, P. R. China*

[3]*Laboratory for Marine Mineral Resources, Qingdao National Laboratory for Marine Science and Technology, Qingdao 266580, P. R. China*

[4]*Department of Seismology, Centre for Scientific Research and Higher Education of Ensenada, Ensenada 22860, Mexico*

Keywords:
Wettability
acoustic response
granular porous media
saturation
ultrasonic experiment

Cited as:
Chen, Y., Fu, L. -Y., Müller, T. M. Direct link between wettability and acoustic signature in granular porous media. Advances in Geo-Energy Research, 2026, 20(1): 16-26.
https://doi.org/10.46690/ager.2026.04.02

Abstract:
Granular porous media are widespread in natural environments. Their mechanical behavior critically depends on the content and distribution of pore fluids, which is of particular significance in subsurface resource recovery processes such as enhanced oil recovery and geological CO_2 sequestration. While evidence shows that wettability affects elastic waves by tuning percolating force chains, a quantitative relation between the contact angle as a measure of wettability and acoustic signatures remains elusive. To overcome this knowledge gap, in this study, ultrasonic experiments were performed on pre-stressed, uniformly mixed water-granular packings composed of quasi-identical beads, spanning a wide range of contact angles across the full saturation range. The different wettability conditions of the granular samples were achieved by using beads of different materials and applying wettability-reversal surface treatments. A critical saturation was established, identified by the emergence of a high frequency liquid-bridge-induced wave in the waveform records, which decreases with increasing contact angle, exhibiting a near-linear correlation in densely packed granular media. To substantiate the experimental findings, the upper and lower bound of this critical saturation were constructed based on a Haines-in-sphere approximation for a regular unit cell. Even though these similar bead packings make up an idealized granular medium, the results provide impetus for inferring the contact angles under *in-situ* conditions using widely deployable acoustic techniques.

1. Introduction

Granular porous media are ubiquitous within the Earth's crust, such as in near-surface soils, aquifers, and fault gouges at depth. The mechanical properties of granular materials are controlled by disordered packing structures that feature heterogeneous interparticle forces and force chain networks (Rintoul and Torquato, 1996; Majmudar and Behringer, 2005; Peters et al., 2005). The presence of fluids alters the mechanical behavior and percolation characteristics of granular media, which has direct consequences for the rate of hydrocarbon recovery in reservoir stimulation (Anderson, 1986; Blunt et al., 2002; Jimenez-Martinez et al., 2016), the spreading of CO_2 plumes (Wang et al., 2016; Bui et al., 2018; Garing and Benson, 2019), and water infiltration into soils (Chang et al., 2009; Lourenco et al., 2018; Assouline and Kamai, 2022). Pore surface wettability exerts a fundamental control on the distribution of fluids within the pore space and their ability to flow relative to each other (AlOmier et al., 2024; Haghani and Berg, 2025) and, as such, is key to understand the

Yandy Scientific Press

*Corresponding author.
E-mail address: yangpu_chen@foxmail.com (Y. Chen); lfu@upc.edu.cn (L.-Y. Fu); tobias@cicese.edu.mx (T. M. Müller).

Received January 5, 2026; revised February 11, 2026; accepted February 26, 2026; available online March 1, 2026.

above processes. For example, in enhanced oil/gas recovery, wettability significantly affects relative permeability and residual trapping, thereby further influencing the efficiency of hydrocarbon recovery in reservoir stimulation (Rao, 1999; Agbalaka et al., 2008; Shao et al., 2025).

Despite its macroscopic implications in subsurface processes, wettability is fundamentally an interfacial property defined at the grain scale. As a physicochemical factor, the wettability of a solid surface essentially describes the preference of one fluid over another to be in contact with the solid surface. For a gas-liquid-solid three-phase system, wettability is quantified by the contact angle θ at the three-phase contact line, described by Young's equation:

$$\cos\theta = \frac{\gamma_{sg} - \gamma_{sl}}{\gamma_{gl}} \tag{1}$$

That is, the contact angle represents the equilibrium state governed by the competition among solid-gas γ_{sg}, solid-liquid γ_{sl}, and gas-liquid γ_{gl} interfacial free energies (De Gennes, 1985; Tadmor, 2004; Quere, 2008). Even though the contact angle provides a simplified means to quantify wettability, the current measurement methods rely on directly observing the spreading angle of a fluid on a solid surface, making *in-situ* measurements in subsurface applications highly challenging (Kwok and Neumann, 1999; Iglauer et al., 2015). This limitation has prompted an increasing interest in indirect approaches for contact angle estimation. Existing methods, such as nuclear magnetic resonance, typically provide qualitative wettability estimation (e.g., water-wet, oil-wet) (Al-Mahrooqi et al., 2003; Su et al., 2018). In contrast, acoustic methods, such as borehole sonic logging and seismic surveys, have been widely applied to investigate pore-fluid distributions (Batzle and Wang, 1992; David et al., 2017; Zhang et al., 2022), which are inherently influenced by wettability. This suggests that acoustic techniques hold a potential for wettability characterization, and recent ultrasonic studies have indeed demonstrated the sensitivity of such methods to wettability changes (Wang et al., 2015; Li et al., 2022; Chen et al., 2025). However, a systematic method of inferring the contact angle from acoustic signatures remains to be developed.

Since surface wettability and stress conditions can be controlled independently in granular porous media, granular packings are particularly advantageous for isolating wettability effects without introducing additional structural complexity. In this context, this study aims to establish a direct link between an acoustic signature and the contact angle in granular packings. For this purpose, ultrasonic experiments are conducted on uniformly mixed water–bead packings confined under low uniaxial pressure, in order to examine acoustic behavior across the full saturation range and over a wide span of contact angles. Specific to this physical system are liquid bridge-induced P-waves (LBIW) emerging at a critical saturation and propagating with the wave speed pertaining to a fully saturated medium (Chen et al., 2025). This critical saturation can be readily identified from measured LBIW velocity-saturation relations. Therefore, it seems straightforward to assume that a correlation between this critical saturation and the contact angle exists as an acoustic signature of wettability. This comprises the main thrust of this paper, and it turns out this assumption indeed proves true. In addition, since the concept of a critical saturation is somewhat abstract, an attempt is made to estimate the lower and upper bounds of this critical saturation, which is performed using a geometrical construction of a regular unit cell (RUC) based on the Haines-in-sphere approximation while taking into account the peculiarities of the granular pack.

The contents of this paper are organized as follows. First, the experimental materials and procedures are outlined. Then, the measured waveforms are reported. To identify wettability-dependent acoustic signatures in granular media, velocity-saturation relations and amplitude spectra are extracted from the original waveform records. A key result is the near-linear correlation between the critical saturation and the contact angle. This correlation is modeled by RUC, which provides the upper and the lower bounds for the critical saturation. In the Discussion section, the experimental results are detailed, providing a potential physical basis for *in-situ* contact angle measurements, and the observations are further interpreted in terms of wettability-controlled force-chain network organization.

2. Materials and methodology

2.1 Sample preparation

Three types of beads (steel, zirconia, and glass) with quasi-identical diameters $d = 500 \pm 50$ μm were used to represent a family of granular media with distinct wettability conditions while maintaining comparable grain geometry. These bead materials differ in intrinsic mechanical properties, including elastic modulus and density. However, this study aims to understand the relative acoustic changes associated with wettability-controlled fluid distribution, rather than the elastic properties of different materials. By normalizing the observations to the dry reference state for each material, the influence of bulk material properties could be minimized, allowing the role of wettability-controlled fluid distribution to be isolated (Chen et al., 2025). To further extend the wettability range, glass beads were treated separately with three different wetting reversal agents (XN534, MD3005, and silane), producing three additional surface wettability conditions. These wetting reversal agents alter the surface wettability by forming nanoscale coatings (tens to hundreds of nanometers thick) on the bead surfaces (Sun et al., 2002; Truong et al., 2011), resulting in a $< 1‰$ change in bead diameter. Because the coating thickness is much smaller than the contact radius (~ 5 μm) between grains, the treated beads fall within the thin-film limit. In this regime, the load-bearing contacts between beads are governed primarily by the elastic properties of the underlying grains rather than by the thin surface coating (Reedy, 2006). Therefore, the coating thickness is negligible and the treatments modify surface wettability without significantly affecting grain geometry and contact mechanics. The wettability conditions of samples were characterized by contact angle measurements (Kwok and Neumann, 1999; Hebbar et al., 2017).

The porosity ϕ of each sample was determined as follows. A known mass m of dry beads was packed into a cylinder w-

Table 1. Parameters of densely packed sample.

Sample	Density (g/cm^3)	Bulk Modulus (GPa)	Shear Modulus (GPa)	Contact Angle (°)	Porosity (%)
Glass bead	2.45	37	26	27 ± 8	37.72
XN534-treated glass bead	2.45	37	26	10 ± 5	37.48
Silane-treated glass bead	2.45	37	26	76 ± 6	38.12
MD3005-treated glass bead	2.45	37	26	110 ± 5	38.83
Zirconia bead	6.05	140	60	54 ± 12	36.75
Steel bead	7.8	160	77	66 ± 10	39.84

Notes: Contact angles measured using the sessile drop method.

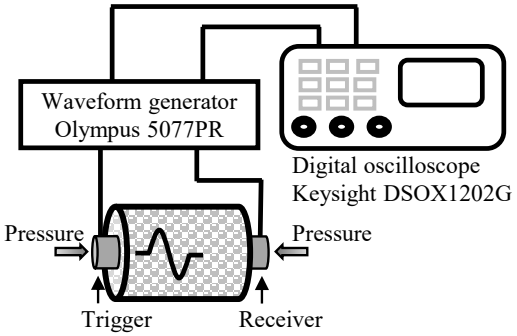

Fig. 1. Schematic experimental setup involving an ultrasonic detection system and a confined bead packing sample under uniaxial pressure.

ith an inner diameter $D = 25.4$ mm and compressed to a uniaxial pressure $\sigma = 400$ kPa. The sample volume was calculated as $V_t = \pi (D/2)^2 L$, where L is the sample length after compaction. The bead volume was computed as $V_s = m/\rho$, where ρ is the bead material density. The porosity was then obtained by $\phi = 1 - V_s/V_t$. Because the beads used in different samples have similar particle sizes, the resulting porosities were comparable across materials and vary only slightly (Table 1).

In total, six densely granular packings with distinct wettability yet comparable pore scale and porosity ($\phi = 38.3 \pm 1.7\%$ at $\sigma = 400$ kPa) were obtained (Table 1). Such densely packed granular media, serving as an idealized model for weakly consolidated rocks, are particularly advantageous for wettability studies. This is because their wettability can be precisely controlled while their geometrical and mechanical parameters remain essentially constant.

2.2 Experimental setup and protocol

Ultrasonic experiments were conducted to record the acoustic response of densely packed beads under a uniaxial pressure with variable water saturation (Fig. 1). The ultrasonic detection system consists of a waveform generator (Olympus 5077PR), a digital oscilloscope (Keysight DSOX1202G), and a pair of piezoelectric transducers (Olympus V103-RM) with broadband frequency centered at 1 MHz and an operating range of 0-2 MHz. This experimental setup is similar to that reported in Chen et al. (2025).

All beads were water-rinsed and oven-dried at 60 °C for 24 h prior to the experiments. Before each measurement, dry beads were premixed with a prescribed amount of water to achieve the desired saturation level. Vigorous mixing was conducted to ensure a uniform distribution of water and to suppress patchy wetting, which are known to introduce pressure gradients between wet and dry regions and cause strong attenuation in acoustic measurements (Muller et al., 2010; Qi et al., 2014; Ba et al., 2017; Yang et al., 2026). Then, the mixture was poured into the cylinder. The uniaxial pressure σ was applied to the sealed bead packing. Transducers were mounted on the two ends of the cylinder for P-wave generation and recording. The initial saturation interval was 10%, and a finer interval of 5% was adopted locally to more accurately determine the critical saturation at which the velocity exhibits an abrupt increase. For each saturation level, the same experimental procedure was repeated five times to minimize the impacts of random distribution and grain size errors.

3. Results

3.1 Waveform records

P-wave records of each uniformly wet sample under variable saturation (S_w) are shown in Fig. 2, and the corresponding first-arrival velocities are tabulated in Table 2. The results indicate a coherent signal with a distinct first arrival under the dry condition ($S_w = 0$). With increasing saturation, the travel-time of the first-arrival is nearly constant (and hence the velocity). Under this condition, the coherent P-waves are barely affected by the presence of water. Once the saturation achieves a critical level, the higher-frequency LBIW emerges and coexists with the coherent wave (Fig. 2). During this coexistence, the two waveforms are clearly distinguishable in both frequency content and arrival time. The appearance of the LBIW is not gradual but emerges abruptly over a small saturation interval, suggesting a threshold-like behavior rather than a continuous evolution with saturation. Note that the saturation at which the LBIW emerges is different under vary-

Table 2. Experimental results of the first-arrival wave velocities for different samples under varied water saturation.

Saturation (%)	Statistics	Velocity (m/s)					
		XN534-treated glass bead	Glass bead	Zirconia bead	Steel bead	Silane-treated glass bead	MD3005-treated glass bead
0	Min	892	932	949	795	1,069	932
	Max	1,023	952	980	826	1,089	952
	Ave	960	942	967	813	1,079	942
10	Min	846	957	920	770	1,048	957
	Max	983	982	957	807	1,073	982
	Ave	918	973	942	791	1,064	973
20	Min	903	958	906	770	1,056	958
	Max	1,023	980	926	790	1,077	980
	Ave	963	963	917	781	1,061	963
30	Min	883	919	961	770	1,040	919
	Max	988	945	966	775	1,066	945
	Ave	936	936	964	773	1,057	936
40	Min	809	924	902	767	1,021	924
	Max	929	947	922	787	1,044	947
	Ave	874	938	917	781	1,035	938
45	Min	/	/	/	/	/	1,917
	Max	/	/	/	/	/	2,080
	Ave	/	/	/	/	/	1,988
50	Min	874	900	933	755	1,875	1,900
	Max	988	953	947	769	2,110	2,135
	Ave	931	931	940	762	2,043	2,068
60	Min	886	884	9,46	775	1,885	2,069
	Max	999	934	959	788	1,978	2,162
	Ave	943	921	952	782	1,938	2,122
70	Min	887	920	931	2,192	1,875	1,992
	Max	1,000	958	944	2,367	2,065	2,182
	Ave	943	943	938	2,294	1,925	2,042
75	Min	/	/	1753	/	/	/
	Max	/	/	1,928	/	/	/
	Ave	/	/	1,855	/	/	/
80	Min	877	2,042	1,922	1,996	1,988	1,988
	Max	994	2,126	2,038	2,112	2,102	2,102
	Ave	936	2,075	1,981	2,054	2,012	2,012
90	Min	1,999	1,908	1,804	2,161	1,859	1,955
	Max	2,239	2,070	1,914	2,271	2,118	2,214
	Ave	2,113	1,998	1,868	2,225	1,936	2,032
100	Min	1,984	1,945	2,017	2,080	/	/
	Max	2,220	2,122	2,124	2,187	/	/
	Ave	2,087	2,032	2,060	2,124	/	/

ing surface wettability conditions and thus defines a critical saturation S_c. This shift in S_c highlights the sensitivity of the LBIW onset to wettability, as the overall packing geometry and loading conditions remain constant. When achieving full saturation ($S_w = 100\%$), the coexistence disappears and only a high-frequency first-arrival remains. Although the mechanical properties of the experimental beads differ, our study focuses on the LBIW under the partially saturated condition, with the coherent wave calibrated against the dry reference records. Following the interpretation of Chen et al. (2025), the coherent wave is propagating through the major force chains formed by direct grain-grain contacts in the densely packed medium. The emergence of LBIWs is attributed to wettability-induced changes in pore-fluid distribution and the associated reorganization of the force-chain network. For example, water tends to adhere to the bead surface under the hydrophilic condition, whereas under the hydrophobic condition, water tends to coalesce into a larger droplet in the pore space. At large contact angles, water droplets preferentially form bridges between glass beads that are not in direct contact, thereby generating extra wave transmission pathways, as illustrated in Fig. 3. Therefore, the onset of LBIW reflects a reorganization of force chains induced by wettability-controlled pore-fluid configurations, suggesting that its emergence at a critical sat-

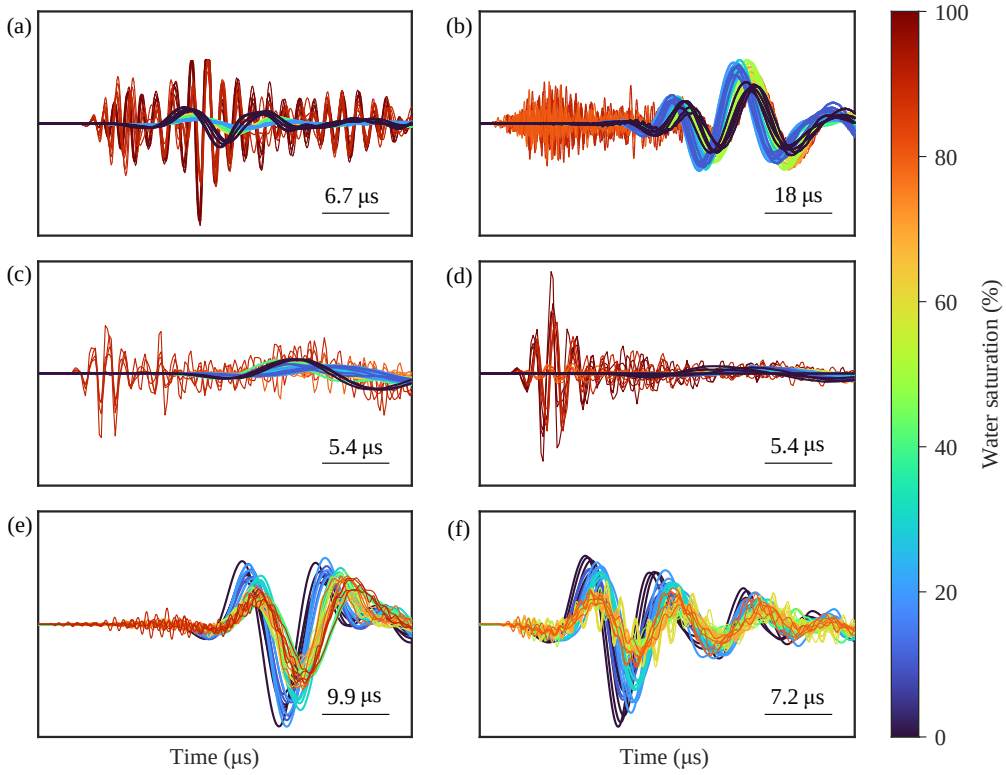

Fig. 2. P-wave records of uniformly wetted samples at different water saturation levels for (a) XN534-treated glass bead packing ($\theta = 10°$), (b) untreated glass bead packing ($\theta = 27°$), (c) zirconia bead packing ($\theta = 54°$), (d) steel bead packing ($\theta = 66°$), (e) silane-treated glass bead packing ($\theta = 76°$), and (f) MD3005-treated glass bead packing ($\theta = 110°$).

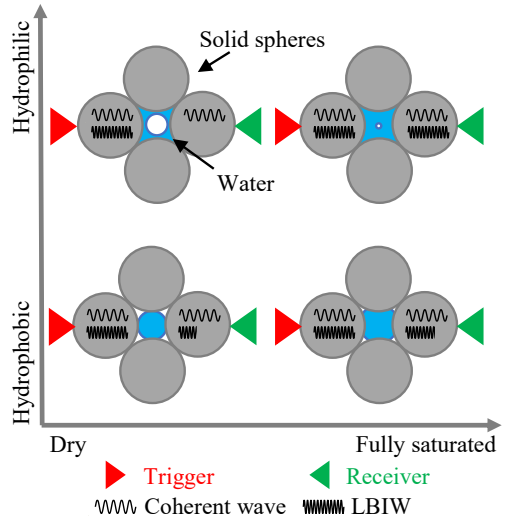

Fig. 3. Schematic of the wave propagation pathway under different saturation levels and varied wettability condition.

uration S_c can be utilized as an indicator of the wettability condition.

In order to characterize the correlation between the wave velocity and water saturation of different samples, the first-arrival velocities were extracted from the waveform records. Fig. 4 shows the variation of first-arrival P-wave velocities of each sample at different water saturation levels. Under partially saturated conditions, both the velocity and the central frequency remain close to those of the dry condition until S_c is reached. Beyond S_c, the velocity rises sharply and rapidly approaches that of full saturation, providing an identifiable feature that can be regarded as diagnostic of the critical saturation. In our experiments, S_c decreases from 90% to 45% as the contact angle increases from 10° to 110°. Of note, a similar abrupt velocity increase has also been observed in earlier studies where pore fluids were uniformly distributed (Domenico, 1977; Knight and Nolen-Hoeksema, 1990). Critical saturation can also be identified in the amplitude spectra (Fig. 5). Once the S_c is reached, the amplitude spectrum exhibits a bimodal distribution, with the low-frequency component resembling the dry condition and the high-frequency component resembling the fully saturated condition (Fig. 5(a) and 5(b)), acting as the frequency-domain evidence that is independent of the travel-time analysis. Interestingly, under hydrophilic conditions, the high-frequency component dominates, whereas under hydrophobic conditions, its amplitude is markedly smaller than that of the low-frequency component. This may be attributed to the reduced adsorption of water on grain surfaces under hydrophobic conditions, leading to enhanced energy dissipation along liquid bridges. This contrast indicates that, even beyond the critical saturation, surface wettability continues to modulate the relative contribution of high-frequency components to the recorded signal. These diagnostic changes in velocity and spectral content provide a means to identify S_c.

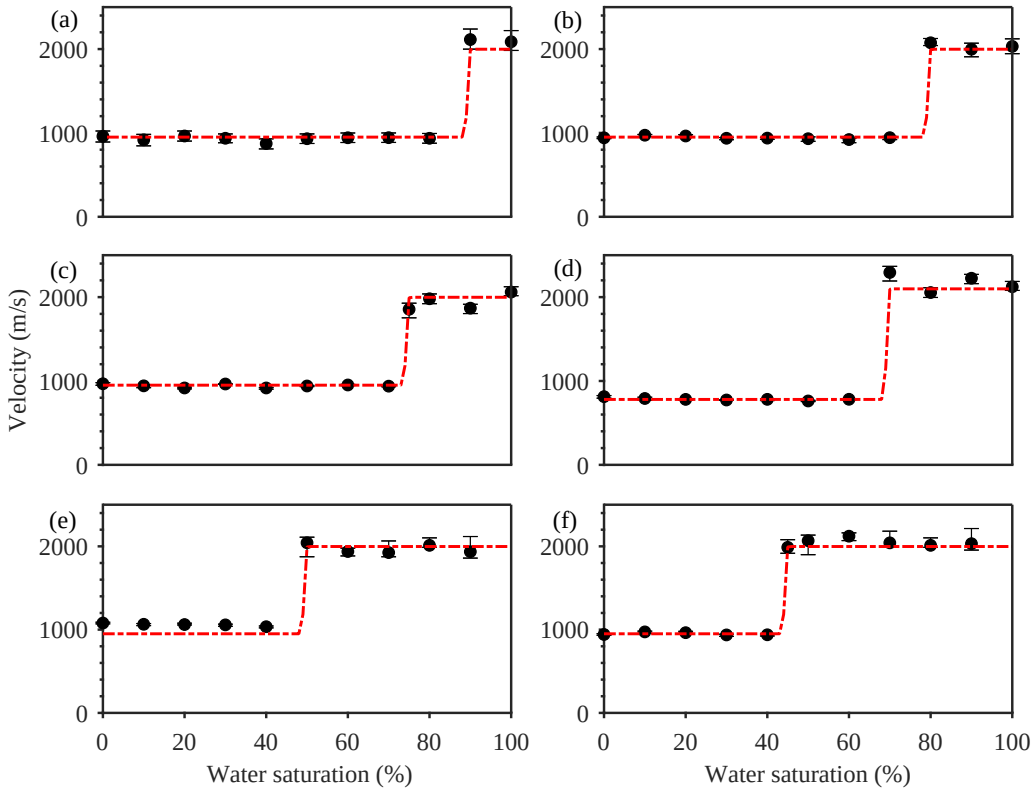

Fig. 4. Velocity-saturation relations derived from first arrivals of (a) XN534-treated glass bead sample ($\theta = 10°$), (b) untreated glass bead sample ($\theta = 27°$), (c) zirconia bead sample ($\theta = 54°$), (d) steel bead sample ($\theta = 66°$), (e) silane-treated glass bead sample ($\theta = 76°$), and (f) MD3005-treated glass bead sample ($\theta = 110°$).

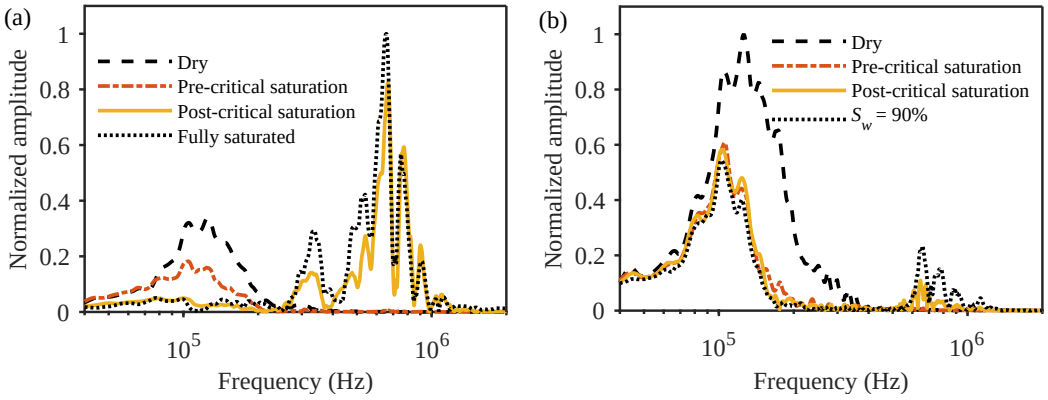

Fig. 5. Normalized amplitude spectra extracted from waveforms at the (a) hydrophilic condition ($\theta = 10°$) and (b) hydrophobic condition ($\theta = 110°$) for different saturation states.

3.2 Critical saturation as a proxy for contact angle

In order to further understand the intrinsic link between acoustic response and fluid distribution tuned by wettability, we extracted the S_c value for different bead packings. This was performed by identifying S_c from the inflection point of each velocity-saturation relations and plotting it against the corresponding contact angle (Fig. 6(a)). Remarkably, despite the differences in the properties of substrates, there is a linear relationship ($R^2 \approx 0.8953$) between the critical saturation S_c and θ:

$$S_c = -0.465\theta + 89.91 \quad (2)$$

This relationship implies that the contact angle can be inferred from S_c. Such a direct correlation is perhaps unexpected and warrants further examination. Instead of correlating S_c with θ, S_c is correlated with $\cos\theta$, which is proportional to the surface free energy (Eq. (1)), as shown in Fig. 6(b). Such a representation provides a stronger linkage between interfacial free energy and S_c, highlighting that wettability fundamentally controls the onset of liquid-bridge formation.

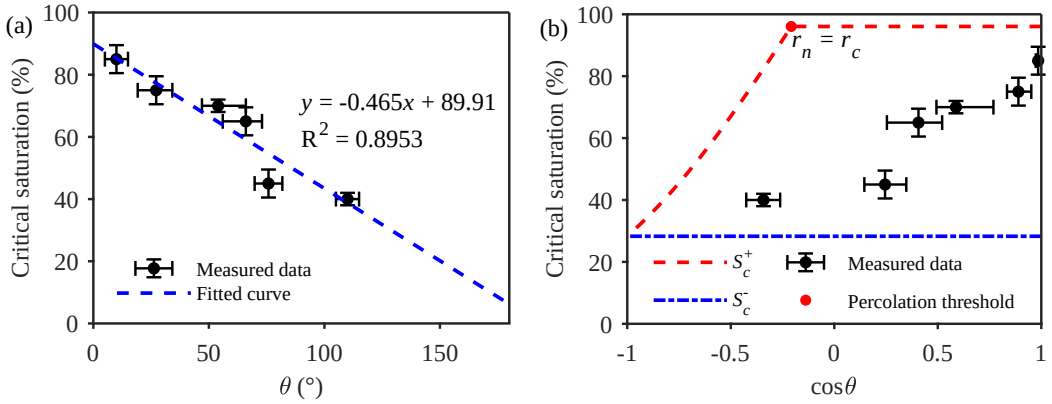

Fig. 6. Correlation between (a) critical saturation and contact angle and (b) critical saturation and $\cos\theta$.

Notably, although $\cos\theta$ in the range of -1 to 0 corresponds to unfavorable wetting interactions and in the range of 0 to 1 corresponds to favorable wetting interactions, a consistent correlation with S_c is still observed. The underlying physical mechanism of this correlation can be attributed to the role of wettability in governing the connectivity of liquid bridges, which will be further elaborated in the following subsection.

3.3 Bounds for critical saturation

While being relevant as an alternative avenue to estimate the contact angle via acoustic measurements, Eq. (2) merely provides a fitting relation between critical saturation and wettability, which prompts us to better understand its physical origin. The onset of the LBIW is thought to be accompanied by the formation of liquid bridges between grains that are not in direct contact. In other words, when a droplet comes into contact with the surrounding spheres, it provides new pathways for wave propagation. Such liquid bridges reinforce localized force chains and allow for enhanced force transmission and thus render a wave velocity pertaining to a saturated porous medium, as predicted by Gassmann's theory (Chen et al., 2025). Hence, it is conceivable that the geometry of the liquid bridge saturating a certain pore volume is an important factor.

RUC represents the smallest portion of a granular packing that fully characterizes both the packing arrangement and the associated pore space. Adopting this RUC concept, all spheres are assumed to be identical, and the cell is bounded by planes passing through the centers of adjacent spheres (see red lines in Fig. 7(b)). The resulting polyhedral cell is therefore the minimum volume that can reproduce the local packing arrangement and the void distribution within the bulk (Graton and Fraser, 1935). The volume of liquid bridges within the pore space can be computed in an idealized case using the Haines-in-sphere approximation. For touching spheres (direct neighbors in contact as expected in densely packed granular media considered here) shown in Fig. 7(a) and 7(b), the volume of a spherical liquid droplet V_n surrounded by n solid spheres is given by:

$$V_n = V_0 - nV_\alpha^c - nV_\beta^c \tag{3}$$

where V_0 denotes the volume of a sphere with droplet radius r_n, while V_α^c and V_β^c correspond to the spherical cap volumes of the droplet and the solid sphere, respectively, when they are in contact. The corresponding expressions are as follows (Tadmor, 2004; Niven, 2006):

$$\begin{aligned} V_0 &= \frac{4\pi}{3} r_n^3 \\ V_\alpha^c &= \frac{\pi r_n^3}{3}\left(2 - 3\cos\alpha + \cos^3\alpha\right) \\ V_\beta^c &= \frac{\pi R^3}{3}\left(2 - 3\cos\beta + \cos^3\beta\right) \\ r_n &= \frac{\sin\beta}{\sin\alpha} R, \quad \alpha + \beta = \eta \end{aligned} \tag{4}$$

where α and β represent the half-filling angle within the droplet and solid sphere, respectively (Fig. 7(b)); $\eta = \pi - \theta$ represents the external contact angle; R denotes the radius of solid spheres. For neighboring spheres in contact, β is given by (Niven, 2006):

$$\sin\left(\frac{\Omega}{2}\right) = \cos\beta + \frac{\sin\beta}{\tan\theta} \tag{5}$$

where Ω stands for the internal angle and α is derived by combining Eqs. (4) and (5).

While the measurement of the interfacial free energies in Eq. (1) is a significant challenge (Al-Yaseri et al., 2016b), Eqs. (3) and (4) can be used to recast the physical problem into a geometric relationship, as θ defines the equilibrium configuration of the solid-liquid-gas interfaces. It should be noted that the RUC pore volume can be expressed as $V_p = \xi R^3$, with ξ a coefficient related to the geometry. The ratio of the droplet volume V_n to the n-sphere unit-cell volume yields the saturation:

$$\frac{V_n}{V_p} = \frac{\pi}{3\xi}\left\{\left(\frac{\sin\beta}{\sin\alpha}\right)^3\left[4 - n\left(2 - 3\cos\alpha + \cos^3\alpha\right)\right] - n\left(2 - 3\cos\beta + \cos^3\beta\right)\right\} \equiv S_c^{\pm} \tag{6}$$

Since the water droplet makes a contact with the spheres dependent on contact angle and pore geometry, Eq. (6) is interpreted as a bounding relation for S_c. In our case, considering $\phi \approx 38\%$, an octahedral RUC was adopted with

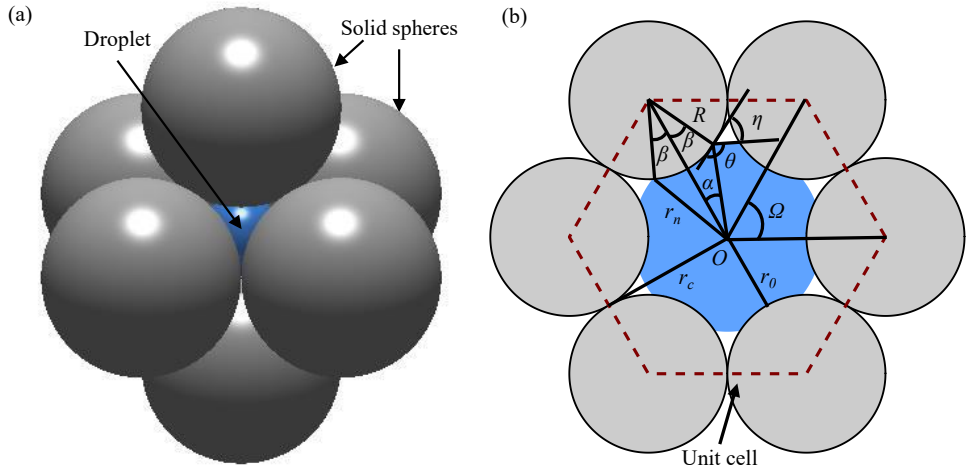

Fig. 7. Schematic of regular unit cell in (a) 3D and (b) 2D, respectively.

$\xi = 1.0525, n = 6$ and $\Omega = 90°$ (Graton and Fraser, 1935; Niven, 2006). The droplet makes contact with each sphere and hence achieves the largest saturation. For this reason, Eq. (6) serves as an upper bound of the critical saturation, denoted as S_c^+. Moreover, S_c^+ exhibits a percolation threshold: When the droplet radius r_n exceeds the distance from the droplet center to the sphere contact r_c (i.e., the pore throat in Fig. 6(b)), adjacent droplets begin to coalesce. In other words, a critical contact angle exists beyond which the pore water coalesces with neighboring droplets and is no longer isolated. The relevant condition is:

$$r_n = \frac{\sin\beta}{\sin\alpha} R \leq r_c \tag{7}$$

where $r_c = \zeta R$, and $\zeta = \sqrt{2/3}$ is also a parameter related to the RUC geometry. The results indicate that for the chosen octahedral RUC, the estimated S_c^+ increases with increasing $\cos\theta$. When $r_n > r_c$, the water volume has exceeded the percolation threshold and S_c^+ no longer varies with $\cos\theta$ (Fig. 6(b), red curve). It should be noted that this geometric construction implicitly suggests the presence of a lower bound for S_c achievable when $r_n = r_0$. Below this limit, no fast pathways are formed to support LBIW propagation.

Under a fully non-wetting condition ($r_n = r_0$), the droplet becomes tangent to the surrounding spheres, yielding the minimum saturation. This can be regarded as the lower bound of the critical saturation, S_c^-, and is depicted in Fig. 6(b) (blue curve). In fact, this lower bound is narrower than the critical saturation found for percolating pendular rings found by Scheel et al. (2008).

Eqs. (4)-(6) demonstrate that the relation between S_c and θ is governed by the RUC geometry. For a given pore structure, R, n, Ω, ξ, and ζ are uniquely defined. Although previous studies have shown that θ also depends on the fluid properties, pore pressure and temperature (Broseta et al., 2012; Al-Yaseri et al., 2016a; Arif et al., 2016), these factors were carefully controlled in our experiments, with a porosity of approximately 38%, uniaxial pressure of 0.4 MPa, and temperature of 20 °C. The relation between critical saturation S_c and contact angle θ, i.e., $S_c = f(\theta)$, can be well approximated by a linear function (Eq. (2)) which is specific for densely packed, quasi-identical granular media. Importantly, the expression of the theoretical upper-bound in Eq. (6) already implies a nonlinear dependence of S_c on θ. Therefore, the near-linear observation arises from the idealized experimental conditions and should be viewed as an empirical representation. For other irregular pore geometries, $f(\theta)$ may be nonlinear. Nevertheless, the key implication that wettability systematically controls the fluid distribution remains true and so does the onset of the acoustically detectable transition, and the specific functional form is expected to be geometry-dependent.

4. Discussion

4.1 Applicability of the geometry model

As noted in the last section, the model is built on a specific geometric configuration, and the results should be interpreted as evidence for a mechanistic relationship: Wettability controls fluid distribution, which in turn leads to the emergence of LBIWs at a critical saturation. Indeed, the model is highly idealized and does not explicitly account for the complex subsurface conditions in reservoirs (such as elevated temperature and stress, or varying fluid types). As evidenced by Eq. (6), the predicted critical saturation depends solely on pore geometry and contact angle. In subsurface reservoir environments, pore-structure is characterized by stress and temperature (Simmons and Cooper, 1978; Zimmerman et al., 1986; Yang et al., 2022). Hence, in principle, the geometric parameters ξ and Ω can be expressed as functions of temperature and pressure. Likewise, the contact angle may vary with fluid type, pore pressure and temperature due to interfacial-chemistry effects (McGuiggan et al., 2007; Arif et al., 2016; Duchemin et al., 2021). Therefore, although the reservoir environment is likely to be more complex, the proposed wettability-dependent fluid distribution mechanism provides a potential physical basis for interpreting or guiding *in-situ* measurements.

4.2 Force chain development pattern

In dry granular media, force chain networks bear most of the mechanical load and thus control the mechanical properties of the dry matrix, including the elastic response to any external acoustic perturbation (Liu and Nagel, 1993; Majmudar and Behringer, 2005). Forces are transmitted through grain contacts, leading to an inhomogeneous force distribution in which a subset of grains carries major loads (major force chains), while the remaining grains sustain minor forces and merely act as network stabilizer (Peters et al., 2005). This inhomogeneous force distribution and the corresponding number density of force chains N_{FC} can be quantified by a simple model for the participation number Π when the average coordination number $\langle Z \rangle$ is known (Makse et al., 2000), such as:

$$\Pi = \frac{2}{\langle Z \rangle} \frac{(1+2\tau)^2}{(1+2\tau^2)} \frac{N_{FC} N_z}{N} \tag{8}$$

where τ denotes a fraction of the major force chain load that is carried by the minor force chain; N_z represents the number of spheres of each force chain; and N is the total number of spheres.

When all grains participate in force chains, i.e., $(N_{FC}N_z)/N \approx 1$, and thus Π approaches its maximum, the system is said to be completely homogenized. The other limiting situation is when only a minimum number of force chains exists ($\Pi \to 0$), so that they become highly localized in space.

This model can be used to support our observations. The coherent wave seen in Fig. 2 reflects the elastic response of the de-localized force-chain network as if the medium was homogenized and only frequencies are transmitted, for which the corresponding wavelength greatly exceeds the grain size. In a dense granular packing under axial pressure ($\sigma = 400$ kPa), we estimate $\langle Z \rangle = 8$ (Chen et al., 2025), $\tau = 0.4$ (Makse et al., 2000) and $(N_{FC}N_z)/N = 1$. This yields the participation number $\Pi \approx 0.62$, which is indeed similar to the value reported in Makse et al. (2000). In contrast, the presence of LBIW means that the system is in the localized force-chain regime, where liquid bridges reinforce the sparse force-chain network. Once this liquid-bridge-reinforced force chain is percolating, it enables a faster propagation pathway supporting the higher-frequency LBIW. While we are unable to directly image such percolating force chains in our experimental setup, it is known that such percolating force chains are instrumental for acoustic pulse transmission (Zhai et al., 2020). However, we have an indirect means to estimate the percolating participation number Π_p: The amplitude spectra provide a qualitative measure of the participation number associated with these percolating chains by assuming that the force-chain network within the matrix remains homogeneous (i.e., $\Pi \approx 0.62$). The higher spectral energy (E = square of spectral amplitudes) ratio between the LBIW E_L and the coherent wave E_c ($\Pi_p = E_L/E_c \times \Pi$) implies a greater percolating participation number. For example, $\Pi_p \approx 0.012$ is relatively low at post-critical saturation (yellow line in Fig. 5(b)), whereas $\Pi_p \approx 0.197$ increases notably at $S_w = 90\%$ (black dotted line in Fig. 5(b)). These values are well below $\Pi \approx 0.62$, i.e., the threshold for homogenization. Under the fully saturated condition (black dotted line in Fig. 5(a)), the coexistence of coherent and LBIW components disappears because the pore-filling water homogenizes the stress distribution, leading to a maximal Π, where all grains and water carry equal stress (hence the measured velocities are consistent with the velocity predicted by Gassmann's theory (Chen et al., 2025)).

5. Conclusions

In this study, ultrasonic measurements under variable saturation were conducted on six granular porous media with distinct wettability conditions, spanning a contact-angle range from 10° to 110°. Our experiments demonstrated that wettability controls ultrasonic wave propagation in granular porous media via its influence on fluid distribution. Although the pore-scale mechanisms of wettability can be highly complex, the results reveal a clear correlation between wettability and acoustic response, manifested by a systematic decrease in critical saturation with increasing contact angle, even exhibiting a near-linear behavior in dense granular packing. Under the controlled experimental conditions of this study, the variations in fluid properties, stress state and temperature were minimized, allowing the critical saturation to be expressed primarily as a function of wettability. A geometric framework based on the RUC was used to link the droplet volume and contact angle, predicting an upper and a lower bound for the critical saturation. For more complex and irregular pore structures, deviations from linearity are expected and the functional dependence of critical saturation on wettability may become more intricate. Altogether, the experimental observations and geometric constraints establish a quantitative basis and bound for estimating contact angles *in-situ* using widely deployed acoustic techniques. Future work should examine the sensitivity of this relationship to variations in fluid properties, stress conditions and temperature, as well as to more heterogeneous pore geometries and natural geological materials.

Acknowledgements

The research has been supported by the National Natural Science Foundation of China (No. 42230803).

Conflicts of interest

The authors declare no competing interest.

References

Agbalaka, C., Dandekar, A. Y., Patil, S. L., et al. The effect of wettability on oil recovery: a review. Paper SPE 114496 Presented at SPE Asia Pacific Oil and Gas Conference and Exhibition, Perth, Australia, 20-22 October, 2008.

Al-Mahrooqi, S. H., Grattoni, C. A., Moss, A. K., et al. An investigation of the effect of wettability on NMR characteristics of sandstone rock and fluid systems. Journal of Petroleum Science and Engineering, 2003, 39(3-4): 389-

398.

AlOmier, A., Hoecherl, M., Cha, D., et al. Experimental investigation of the impact of mixed wettability on pore-scale fluid displacement: A microfluidic study. ACS Applied Materials & Interfaces, 2024, 16(50): 69165-69179.

Al-Yaseri, A. Z., Lebedev, M., Barifcani, A., et al. Receding and advancing (CO_2 + brine + quartz) contact angles as a function of pressure, temperature, surface roughness, salt type and salinity. The Journal of Chemical Thermodynamics, 2016a, 93: 416-423.

Al-Yaseri, A. Z., Roshan, H., Lebedev, M., et al. Dependence of quartz wettability on fluid density. Geophysical Research Letters, 2016b, 43(8): 3771-3776.

Anderson, W. G. Wettability literature survey- part 1: Rock-/oil/brine interactions and the effects of core handling on wettability. Journal of Petroleum Technology, 1986, 38(10): 1125-1144.

Arif, M., Al-Yaseri, A. Z., Barifcani, A., et al. Impact of pressure and temperature on CO_2-brine-mica contact angles and CO_2-brine interfacial tension: Implications for carbon geo-sequestration. Journal of Colloid and Interface Science, 2016, 462: 208-215.

Assouline, S., Kamai, T. Unique relationship between rate and cumulative flow: A property of infiltration and evaporation in soils. Geophysical Research Letters, 2022, 49(6): E2021GL097449.

Ba, J., Xu, W., Fu, L., et al. Rock anelasticity due to patchy saturation and fabric heterogeneity: A double double-porosity model of wave propagation. Journal of Geophysical Research: Solid Earth, 2017, 122(3): 1949-1976.

Batzle, M., Wang, Z. Seismic properties of pore fluids. Geophysics, 1992, 57(11): 1396-1408.

Blunt, M. J., Jackson, M. D., Piri, M., et al. Detailed physics, predictive capabilities and macroscopic consequences for pore-network models of multiphase flow. Advances in Water Resources, 2002, 25(8-12): 1069-1089.

Broseta, D., Tonnet, N., Shah, V. Are rocks still water-wet in the presence of dense CO_2 or H_2S? Geofluids, 2012, 12(4): 280-294.

Bui, M., Adjiman, C. S., Bardow, A., et al. Carbon capture and storage (CCS): The way forward. Energy & Environmental Science, 2018, 11(5): 1062-1176.

Chang, L., Chen, H., Shan, H., et al. Effect of connectivity and wettability on the relative permeability of NAPLs. Environmental Geology, 2009, 56(7): 1437-1447.

Chen, Y., Fu, L., Müller, T. M., et al. Laboratory insights on acoustics of granular porous media with wettability changes. Geophysics, 2025, 90(6): MR429-MR440.

David, C., Barnes, C., Desrues, M., et al. Ultrasonic monitoring of spontaneous imbibition experiments: Acoustic signature of fluid migration. Journal of Geophysical Research: Solid Earth, 2017, 122(7): 4931-4947.

De Gennes, P. G. Wetting: Statics and dynamics. Reviews of Modern Physics, 1985, 57(3): 827-863.

Domenico, S. N. Elastic properties of unconsolidated porous sand reservoirs. Geophysics, 1977, 42(7): 1339-1368.

Duchemin, B., Cazaux, G., Gomina, M., et al. Temperature-dependence of the static contact angle: A transition state theory approach. Journal of Colloid and Interface Science, 2021, 592: 215-226.

Garing, C., Benson, S. M. CO_2 wettability of sandstones: Addressing conflicting capillary behaviors. Geophysical Research Letters, 2019, 46(2): 776-782.

Graton, L. C., Fraser, H. J. Systematic packing of spheres: With particular relation to porosity and permeability. The Journal of Geology, 1935, 43(8): 785-909.

Haghani, R., Berg, C. F. A review on wettability characterization from 3D pore-scale images. Transport in Porous Media, 2025, 152(11): 93.

Hebbar, R. S., Isloor, A. M., Ismail, A. F. Contact angle measurements, in Membrane Characterization, edited by N. Hilal, A. F. Ismail, T. Matsuura, and D. Oatley-Radcliffe, Elsevier, Amsterdam, pp. 219-255, 2017.

Iglauer, S., Pentland, C. H., Busch, A. CO_2 wettability of seal and reservoir rocks and the implications for carbon geo-sequestration. Water Resources Research, 2015, 51(1): 729-774.

Jiménez-Martínez, J., Porter, M. L., Hyman, J. D., et al. Mixing in a three-phase system: Enhanced production of oil-wet reservoirs by CO_2 injection. Geophysical Research Letters, 2016, 43(1): 196-205.

Knight, R., Nolen-Hoeksema, R. A laboratory study of the dependence of elastic wave velocities on pore scale fluid distribution. Geophysical Research Letters, 1990, 17(10): 1529-1532.

Kwok, D. Y., Neumann, A. W. Contact angle measurement and contact angle interpretation. Advances in Colloid and Interface Science, 1999, 81(3): 167-249.

Li, J. X., Rezaee, R., Müller, T. M., et al. Wettability-dependent wave velocities and attenuation in granular porous media. Geophysics, 2022, 87(4): MR177-MR187.

Liu, C., Nagel, S. R. Sound in a granular material: Disorder and nonlinearity. Physical Review B, 1993, 48(21): 15646-15650.

Lourenço, S. D. N., Saulick, Y., Zheng, S., et al. Soil wettability in ground engineering: Fundamentals, methods, and applications. Acta Geotechnica, 2018, 13(1): 1-14.

Majmudar, T. S., Behringer, R. P. Contact force measurements and stress-induced anisotropy in granular materials. Nature, 2005, 435(7045): 1079-1082.

Makse, H. A., Johnson, D. L., Schwartz, L. M. Packing of compressible granular materials. Physical Review Letters, 2000, 84(18): 4160-4163.

McGuiggan, P. M., Wallace, J. S., Smith, D. T., et al. Contact mechanics of layered elastic materials: Experiment and theory. Journal of Physics D: Applied Physics, 2007, 40(19): 5984-5994.

Müller, T. M., Gurevich, B., Lebedev, M. Seismic wave attenuation and dispersion resulting from wave-induced flow in porous rocks – A review. Geophysics, 2010, 75(5): 75A147-75A164.

Niven, R. K. Force stability of pore-scale fluid bridges and ganglia in axisymmetric and non-axisymmetric configurations. Journal of Petroleum Science and Engineering, 2006, 52(1-4): 1-18.

Peters, J. F., Muthuswamy, M., Wibowo, J., et al. Charac-

terization of force chains in granular material. Physical Review E, 2005, 72(4): 041307.

Qi, Q., Müller, T. M., Gurevich, B., et al. Quantifying the effect of capillarity on attenuation and dispersion in patchy-saturated rocks. Geophysics, 2014, 79(5): WB35-WB50.

Quéré, D. Wetting and roughness. Annual Review of Materials Research, 2008, 38(1): 71-99.

Rao, D. N. Wettability effects in thermal recovery operations. SPE Reservoir Evaluation & Engineering, 1999, 2(5): 420-430.

Reedy, E. D. Thin-coating contact mechanics with adhesion. Journal of Materials Research, 2006, 21(10): 2660-2668.

Rintoul, M. D., Torquato, S. Metastability and crystallization in hard-sphere systems. Physical Review Letters, 1996, 77(20): 4198-4201.

Scheel, M., Seemann, R., Brinkmann, M., et al. Morphological clues to wet granular pile stability. Nature Materials, 2008, 7(3): 189-193.

Shao, J., Wang, Z., Huang, B., et al. Wetting and injecting effects on CO_2 distribution: Pore-scale micromodel and simulation. Advances in Geo-Energy Research, 2025, 18(2): 99-108.

Simmons, G., Cooper, H. W. Thermal cycling cracks in three igneous rocks. International Journal of Rock Mechanics and Mining Sciences & Geomechanics Abstracts, 1978, 15(4): 145-148.

Sun, C., Aston, D. E., Berg, J. C. Structural evolution of octyltriethoxysilane films on glass surfaces during annealing at elevated temperature. Journal of Colloid and Interface Science, 2002, 248(1): 96-102.

Su, S., Jiang, Z., Shan, X., et al. The wettability of shale by NMR measurements and its controlling factors. Journal of Petroleum Science and Engineering, 2018, 169: 309-316.

Tadmor, R. Line energy and the relation between advancing, receding, and young contact angles. Langmuir, 2004, 20(18): 7659-7664.

Truong, Q. H., Lee, J., Dong, Y., et al. Capillary induced small-strain stiffness for hydrophilic and hydrophobic granular materials: Experimental and numerical studies. Soils and Foundations, 2011, 51(4): 713-721.

Wang, S., Tokunaga, T. K., Wan, J., et al. Capillary pressure-saturation relations in quartz and carbonate sands: Limitations for correlating capillary and wettability influences on air, oil, and supercritical CO_2 trapping. Water Resources Research, 2016, 52(8): 6671-6690.

Wang, Z., Schmitt, D. R., Wang, R. Does wettability influence seismic wave propagation in liquid-saturated porous rocks? Geophysical Journal International, 2015, 203(3): 2182-2188.

Yang, B., Ba, J., Zhang, L., et al. Seismic wave propagation in partially saturated double-porosity media: The role of capillarity. Advances in Geo-Energy Research, 2026, 19(1): 72-81.

Yang, J., Fu, L., Zhang, Y., et al. Temperature- and pressure-dependent pore microstructures using static and dynamic moduli and their correlation. Rock Mechanics and Rock Engineering, 2022, 55(7): 4073-4092.

Zhai, C., Herbold, E. B., Hurley, R. C. The influence of packing structure and interparticle forces on ultrasound transmission in granular media. Proceedings of the National Academy of Sciences of the United States of America, 2020, 117(28): 16234-16242.

Zhang, L., Ba, J., Carcione, J. M., et al. Seismic wave propagation in partially saturated rocks with a fractal distribution of fluid-patch size. Journal of Geophysical Research: Solid Earth, 2022, 127(2): E2021JB023809.

Zimmerman, R. W., Somerton, W. H., King, M. S. Compressibility of porous rocks. Journal of Geophysical Research: Solid Earth, 1986, 91(B12): 12765-12777.